

Self-Reinforcing Degradation of Solution-Processed Small-Molecule OLEDs: Excited-States and Molecular Interactions as Key Triggers

Eonji Cha, Junwon Jeon, Hyeon Woo Kim, Han Uk Lee, Joo Yoon Woo, Jun-Su Yeo, Hyuk Bin Kwon, Sung Beom Cho,* and Tae-Hee Han*

Solution-processed organic light-emitting diodes (SOLEDs) are promising candidates for cost-efficient and scalable displays, if their operational stability can be increased to match that of thermal-evaporation-processed OLEDs. This study provides a comprehensive analysis of the fundamental degradation mechanisms in SOLEDs. This work reveals a self-reinforcing degradation cycle in which charge accumulation in molecular aggregates and hetero-interfaces strengthens exciton-polaron interactions, thereby promoting further molecular aggregation and nonradiative exciton annihilation. This work applies material engineering strategies, including the use of host-guest combination with minimal intermolecular interactions, modification of the hole injection interface, and suppression of self-reinforcing degradation pathway to obtain SOLEDs that have luminous efficiency exceeding 100 cd A^{-1} and a half lifetime of over 700 h. These findings establish a strategic approach to increase SOLED efficiency and longevity, while offering insights into the design principles required for next-generation organic optoelectronic devices.

1. Introduction

Solution-processed organic light-emitting diodes (SOLEDs) offer several advantages over thermally-evaporated OLEDs (EOLEDs),

E. Cha, J. Jeon, H. B. Kwon, T.-H. Han
 Department of Display Science and Engineering
 Hanyang University
 222 Wangsimni-ro, Seongdong-gu, Seoul 04763, Republic of Korea
 E-mail: taeheehan@hanyang.ac.kr
 H. W. Kim, H. U. Lee, S. B. Cho
 Department of Materials Science and Engineering
 Ajou University
 206 World Cup-ro, Yeongtong-gu, Suwon-si 16499, Republic of Korea
 E-mail: csb@ajou.ac.kr
 J. Y. Woo, J.-S. Yeo, T.-H. Han
 Division of Materials Science and Engineering
 Hanyang University
 222 Wangsimni-ro, Seongdong-gu, Seoul 04763, Republic of Korea

The ORCID identification number(s) for the author(s) of this article can be found under <https://doi.org/10.1002/adfm.202508146>

© 2025 The Author(s). Advanced Functional Materials published by Wiley-VCH GmbH. This is an open access article under the terms of the Creative Commons Attribution License, which permits use, distribution and reproduction in any medium, provided the original work is properly cited.

DOI: [10.1002/adfm.202508146](https://doi.org/10.1002/adfm.202508146)

such as lower production costs and compatibility with large-area manufacturing.^[1] Pixel separation in EOLED production requires use of fine metal masks, which complicates the development of large-area and high-resolution displays.^[2] In contrast, SOLEDs fabricated using inkjet printing technology, which applies materials drop-on-demand to pattern pixels, can reduce production cost by $\approx 25\%$ and be compatible with large-area mother glasses.^[1,3] Furthermore, SOLEDs facilitate fabrication of sub-pixels that emit red, green and blue light, and thereby enable top-emission device architectures and increase the aperture ratio of display panels compared to those of EOLEDs.^[1,4-7]

Although the luminous efficiencies of SOLEDs have been significantly improved by using triplet-harvesting phosphorescent or thermally-activated delayed-fluorescent

guest molecules,^[8-17] which enable 100% internal quantum efficiency, the operational stability of SOLEDs remains far below those of commercialized EOLEDs.^[1] Additionally, SOLEDs undergo significant roll-off in luminous efficiency at a high luminescence; this drawback limits their practical applications in displays and lighting.^[1,10]

In general, the operational stability of OLEDs strongly depends on electron-hole charge balance during device operation, because imbalanced charge injection/transport can lead to accumulation of space charges at the hetero-interfaces in the device.^[10,18-20] This accumulation of excited species causes both exciton-exciton and exciton-charge annihilation, which accelerate degradation of materials and devices, and also causes significant efficiency roll-off.^[20] Specifically, the energy transfer between positive polaron and exciton generates unstable positive polarons, which in turn increase molecular aggregation of materials.^[21,22] This effect is more pronounced in solution-processed organic thin films than in thermally-evaporated organic films. In SOLEDs, redissolution of underlying layers leads to a relatively large energy barrier at the charge-injection interfaces, so achieving good charge balance in SOLEDs is a challenge.^[8,23] Additionally, electrostatic interactions between organic conjugated molecules occur easily during solution processing of SOLEDs; the resulting molecular aggregation and consequent electromer formation during device operation lead to a greater effect of exciton annihilation and device

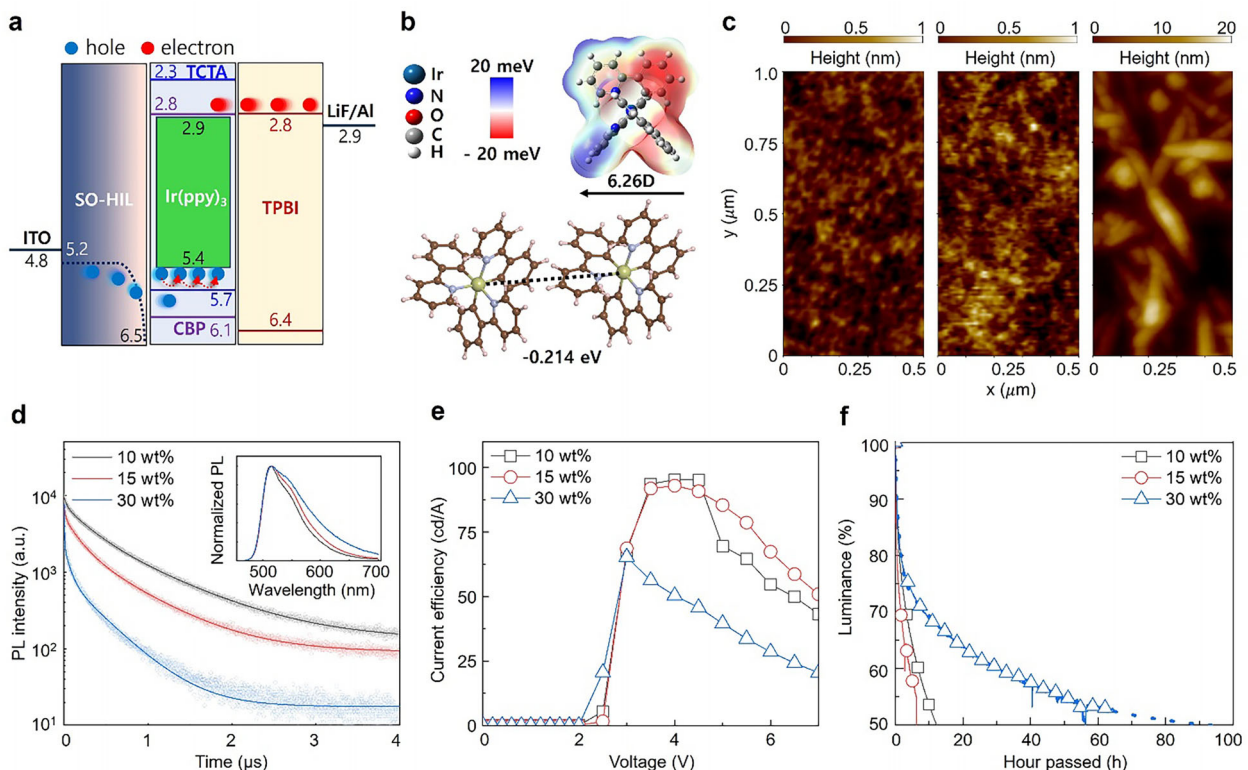


Figure 1. a) Energy level diagram of solution-processed organic light-emitting diodes (SOLEDs) that used homoleptic Ir complex $\text{Ir}(\text{ppy})_3$, and mixed-host of TCTA:CBP. b) Dipole moment and intermolecular interaction energy of $\text{Ir}(\text{ppy})_3$. c) Atomic force microscope (AFM) images and d) time-resolved photoluminescence (TRPL) spectra (inset: steady-state PL) of solution-processed TCTA:CBP: $\text{Ir}(\text{ppy})_3$ films with $\text{Ir}(\text{ppy})_3$ weight ratios of 10, 15, and 30 wt%. e) Current efficiency versus voltage characteristics of SOLEDs with $\text{Ir}(\text{ppy})_3$ concentrations of 10, 15, and 30 wt%. f) Luminance decay curve of SOLEDs with different $\text{Ir}(\text{ppy})_3$ concentrations under constant-current operation.

degradation than in EOLEDs.^[1,24,25] The tendency for molecular packing resulting from the thermal treatment of thin films also significantly affects the characteristics of SOLEDs. Therefore, to improve both efficiency and stability of SOLEDs, the chemical structure and thermal properties of both host and guest molecules are additional key factors that must be considered.

Poly(3,4-ethylenedioxythiophene) polystyrene sulfonate (PEDOT:PSS) is widely used as a solution-processable polymeric hole injection layer (HIL) in SOLEDs, and the polymeric HIL also has a significant influence on efficiency and operational stability of device.^[19,20,23] Its strong acidity ($1.0 \leq \text{pH} \leq 2.5$)^[26,27] causes etching of the underlying metal oxide transparent electrode (e.g., indium-tin-oxide, ITO), leading to the release of metal species that diffuse into the organic emitting layer (EML) and act as nonradiative quenching centers.^[28] These species significantly deteriorate device efficiency and operational stability.^[23,28] PEDOT:PSS also has an insufficient ionization potential ($\approx 4.8 \leq \text{IP} \leq 5.2 \text{ eV}$), so a large energy barrier forms at the hole-injection interface with the EML of phosphorescent/delayed fluorescent OLEDs that use wide bandgap host molecules.^[9,23] This barrier results in charge accumulation at the HIL/EML interface, highlighting the importance of interfacial engineering for improving device performance and reliability.

In this study, we conducted a systematic investigation of the key factors that affect both efficiency and operational degradation of SOLEDs. By analyzing chemical structure, molecular interac-

tions, charge balance, and charge-injection interface properties, we developed an understanding of the degradation mechanisms that affect SOLEDs and proposed strategic methods to improve their efficiency and longevity simultaneously. Our findings emphasize that device degradation is strongly affected by interactions between excited states, and by the consequent molecular interactions.

2. Results and Discussion

2.1. Molecular Properties of Guest

For this systematic study of factors that influence SOLED characteristics, a simple device structure composed of HIL/EML/electron transporting layer (ETL) (Figure 1a) was used, to minimize solution-processing complications related to intermixing or redissolution of underlying layers. This approach achieves high luminous efficiency despite its simplicity.^[8] The mixed-host composition of two host materials was optimized with a hole-transporting host molecule, 4,4',4''-tris(N-carbazolyl)-triphenylamine (TCTA):ambipolar host molecule, 4,4'-Bis(N-carbazolyl)-1,1'-biphenyl (CBP) ratio of 3:7 (wt:wt) to achieve balanced charge transport and higher luminous efficiency ($>100 \text{ cd A}^{-1}$) compared to the single-host EML that uses only TCTA ($\approx 65 \text{ cd A}^{-1}$) (Figures S1 and S2, Supporting Information).

The study investigates the effects of molecular structure and concentration of phosphorescent guest molecules on SOLED characteristics. Three green phosphorescent iridium (III) complexes were used: (1) homoleptic tris(2-phenylpyridine)iridium ($\text{Ir}(\text{ppy})_3$); (2) heteroleptic bis[2-(2-pyridinyl-N)phenyl-C(acetylacetato)iridium(III) ($\text{Ir}(\text{ppy})_2(\text{acac})$); and (3) methyl-substituted homoleptic tris[2-(*p*-tolyl)pyridine]iridium ($\text{Ir}(\text{mpy})_3$). Density functional theory (DFT) calculation estimated that $\text{Ir}(\text{ppy})_3$ has a molecular dipole moment of 6.26 D, and an intermolecular binding energy of -0.214 eV (Figure 1b); both are the highest in magnitude among the three guest molecules used in this study.

Guest concentration affected the surface morphology within the EML film. Mixing a high concentration of 30 wt% $\text{Ir}(\text{ppy})_3$ to host molecules predominantly led to formation of needle-like aggregates (Figure 1c), which function as centers for triplet exciton accumulation, and thereby worsen triplet-triplet annihilation and triplet-polaron annihilation.^[29] Exciton quenching in these aggregated guests significantly reduces the photoluminescence (PL) lifetime (Figure 1d) and induces a red-shift in the PL spectrum (inset of Figure 1d). This change also demonstrates significant guest molecule aggregation within the film, because the formation of aggregates reduces the bandgap compared to the isolated molecule.^[30] The increase in refractive index at $\lambda = 450$ nm further supports the formation of guest aggregates (Figure S3, Supporting Information).

Although molecular aggregation decreases radiative recombination from the phosphorescent guest molecules, it facilitates hole injection and transport within the EML due to the lower highest occupied molecular orbital (HOMO) level of $\text{Ir}(\text{ppy})_3$ (≈ 5.4 eV)^[10] relative to host materials (TCTA > 5.7 eV), enabling direct trapping into guest molecules from the HIL (IP of PEDOT:PSS: ≈ 5.2 eV) and effective percolation for hopping transport of holes between guest molecules at high concentrations (Figure 1a).^[8] Therefore, even though the luminous efficiency decreased from 95.2 cd A⁻¹ at 10 wt% $\text{Ir}(\text{ppy})_3$ to 65.3 cd A⁻¹ at 30 wt% $\text{Ir}(\text{ppy})_3$, the current density and luminance significantly increased at 30 wt% $\text{Ir}(\text{ppy})_3$ (Figure 1e; Figure S4, Supporting Information). The improved hole injection and transport enhance the charge balance between holes and electrons within the EML, as reflected in the capacitance-voltage (C-V) characteristics of the SOLEDs (Figures S5 and S6, Table S1, Supporting Information). A reduced peak capacitance, C_{peak} , indicates lowered charge accumulation and improved charge balance in the device,^[10,19,31] which also extended the half-lifetime (T_{50}) of the SOLEDs from ≈ 12 h at 10 wt% $\text{Ir}(\text{ppy})_3$ to 95 h at 30 wt% $\text{Ir}(\text{ppy})_3$ under constant current operation (Figure 1f).

The chemical structure of phosphorescent guest molecules significantly influences their aggregation tendencies at high concentrations. $\text{Ir}(\text{ppy})_3$ has a homoleptic configuration that has a high dipole moment (6.26 D) and high intermolecular binding energy (-0.214 eV), which induce aggregation, whereas $\text{Ir}(\text{ppy})_2(\text{acac})$ has a heteroleptic structure that has a low dipole moment (≈ 2.61 D) and low intermolecular interaction (-0.047 eV), which together effectively suppress molecular aggregation (Figure 2a). The primary structural distinction between $\text{Ir}(\text{ppy})_3$ and $\text{Ir}(\text{ppy})_2(\text{acac})$ is that $\text{Ir}(\text{ppy})_2(\text{acac})$ bears an acetylacetone group, and this structural difference strongly affects the change in dipole moment and molecular interaction

energy as the guest concentration increases. The symmetrical molecular geometry of $\text{Ir}(\text{ppy})_3$ reduces the directionality of non-covalent interactions with surrounding host molecules, resulting in weakened host-guest interactions.^[32,33] In such cases, guest molecules are more likely to experience stronger Keesom interactions with each other rather than with host molecules, leading to a predominance of guest-guest aggregation.^[33] Therefore, $\text{Ir}(\text{ppy})_3$ exhibits a stronger tendency toward guest-guest molecular aggregation due to the combined effects of its high dipole moment and molecular geometry (Figures S7 and S8, Supporting Information). The presence of methyl groups at the meta position of the phenyl rings also reduces intermolecular interactions between $\text{Ir}(\text{mpy})_3$ guest molecules (-0.117 eV) compared to those between $\text{Ir}(\text{ppy})_3$ s (-0.214 eV),^[34,35] and the three methyl groups attached to the ppy ligands in $\text{Ir}(\text{mpy})_3$ improve the solubility of the guest molecules in organic solvents.^[36] As a result, molecules of both $\text{Ir}(\text{ppy})_2(\text{acac})$ and $\text{Ir}(\text{mpy})_3$ did not cause any significant morphological variation as their concentration increased in blend EML film (Figure 2b; Figure S9, Supporting Information). Furthermore, mixing various concentrations of $\text{Ir}(\text{ppy})_2(\text{acac})$ or $\text{Ir}(\text{mpy})_3$ caused minimal variation in root-mean-square roughness and refractive index (≈ 1.71 at 450 nm) in the thin films (Figure 2c; Figure S10, Supporting Information).

An increase in the concentration of both $\text{Ir}(\text{ppy})_2(\text{acac})$ and $\text{Ir}(\text{mpy})_3$ also improves direct hole injection into the guest molecules and facilitates hopping transport through the guest molecules. As a result, SOLEDs with 30 wt% of either $\text{Ir}(\text{ppy})_2(\text{acac})$ or $\text{Ir}(\text{mpy})_3$ had decreased threshold voltage V_{th} (i.e., earlier hole injection), reduced C_{peak} (i.e., reduced charge accumulation), and lower voltage V_{peak} at C_{peak} (i.e., recombination of electrons and holes begins to dominate at a lower voltage, and charge transport in the device is more balanced) (Figure 2d,e; Figures S11 and S12, Supporting Information).^[19]

The suppressed guest aggregation at high concentration enables balanced charge transport, reduced charge accumulation in the EML and mitigated non-radiative recombination, leading to extended SOLEDs T_{50} of 237 h and 275 h with $\text{Ir}(\text{ppy})_2(\text{acac})$ and $\text{Ir}(\text{mpy})_3$, respectively, compared to ≈ 95 h for $\text{Ir}(\text{ppy})_3$ (Figure 2f,g; Figure S13, Supporting Information). These results indicate that charge accumulation at the interfaces can be effectively reduced at high guest concentrations, which in turn mitigates interactions between accumulated excited-state species and excitons within the EML (Figures S6 and S14, Tables S1 and S2, Supporting Information).^[37,38] However, the chemical structure of the guest molecules determines intermolecular electrostatic dipole interactions, so to retain the luminous efficiency and improve operational stability in SOLEDs, low dipole moment and intermolecular interactions are necessary.

2.2. Molecular Properties of Host

Molecules in solution-processed films are not as tightly packed as those in vacuum deposited films, and solvent impurities easily remain within the films.^[24,39] Therefore, solution processing generally involves an extra step in which the formed film is baked or cured at elevated temperatures to eliminate residual solvents. The conditions under which the EML is processed significantly affect

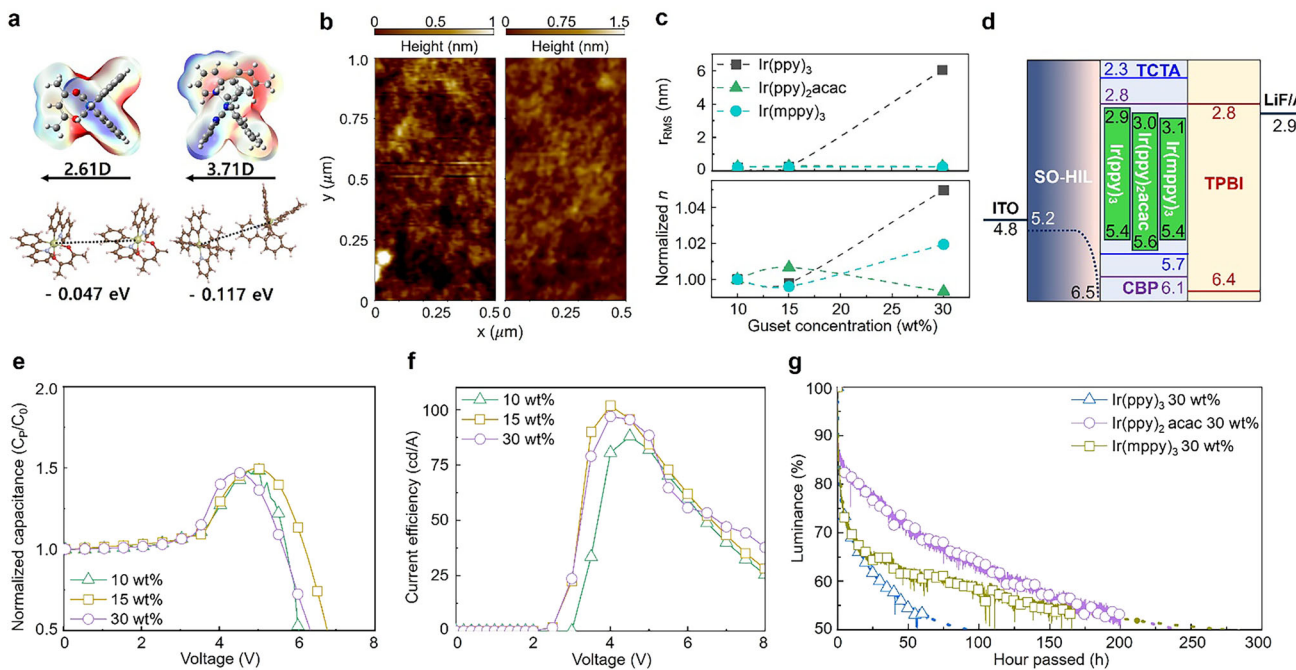


Figure 2. a) Dipole moment and intermolecular interaction energy of $\text{Ir}(\text{ppy})_2(\text{acac})$ and $\text{Ir}(\text{mppy})_3$. b) Atomic force microscope (AFM) images of solution-processed emitting layer (TCTA:CBP:guest) films with 30 wt% of $\text{Ir}(\text{ppy})_2(\text{acac})$ and 30 wt% of $\text{Ir}(\text{mppy})_3$. c) Evolution of root-mean-square roughness and normalized refractive index for solution-processed emitting layer (TCTA:CBP:guest [$\text{Ir}(\text{ppy})_3$, $\text{Ir}(\text{ppy})_2(\text{acac})$ or $\text{Ir}(\text{mppy})_3$]) with guest concentrations of 10, 15, and 30 wt%. d) Energy level diagram of SOLEDs with $\text{Ir}(\text{ppy})_3$, $\text{Ir}(\text{ppy})_2(\text{acac})$ or $\text{Ir}(\text{mppy})_3$ guest. e) Normalized capacitance versus voltage and f) current efficiency versus voltage characteristics of SOLEDs with $\text{Ir}(\text{ppy})_2(\text{acac})$ concentrations of 10, 15, and 30 wt%. g) Luminance-decay over time of SOLEDs with 30 wt% concentration for $\text{Ir}(\text{ppy})_3$, $\text{Ir}(\text{ppy})_2(\text{acac})$ and $\text{Ir}(\text{mppy})_3$ guest under constant-current operation.

the film morphology, interlayer interfaces, and consequently, the optical and electrical properties of the device.

To investigate the influence of host molecule structure and thermal treatment on solution-processed host-guest thin films, a comparative study was conducted using two types of EML: one consisting solely of TCTA, which has a spherical molecular shape and a high glass transition temperature, $T_g \approx 152^\circ\text{C}$,^[40] and the other a mixed-host EML (TCTA:CBP = 3:7) mainly composed of CBP, which has a relatively planar molecular shape and a low $T_g \approx 62^\circ\text{C}$.^[41] Thermal annealing increased current density but slightly decreased luminance at a given applied voltage of TCTA single-host SOLEDs (Figure S15a, Supporting Information); this result occurs because thermal annealing increases the packing density of organic molecules in the thin film. The increased molecular packing facilitates charge-carrier hopping transport, but the reduced intermolecular distance could lead to an increase in the non-radiative exciton-annihilation process within the film, and thereby decrease the luminance of the SOLEDs with annealed films. However, the device that used TCTA:CBP showed both a significant drop in luminance and a decrease in current density upon thermal annealing. (Figure S15b, Supporting Information).

To quantify the extent of molecular aggregation and crystallization of TCTA and CBP at different temperatures, molecular dynamics (MD) simulations were performed for TCTA-only, CBP-only, and TCTA:CBP mixed-host systems. The distribution of molecules and the radial distribution function of the distances between the centers-of-mass of each molecule were analyzed af-

ter 10 ns at 25 °C (298 K; room temperature) and 110 °C (383 K) (Figure 3a–c; Figures S16–S24, Supporting Information). The TCTA molecules showed only a slight reduction in intermolecular distances with minimal change in molecular distribution after 10 ns (Figure 3a,b; Figures S16 and S17, Supporting Information). In contrast, CBP showed a pronounced increase in both the number and proportion of molecules with short center-of-mass distances (Figure 3a,c; Figures S18 and S19, Supporting Information); this change was more intense at 110 °C than at 25 °C (Figure S20, Supporting Information). In simulations of the case with 25 TCTA molecules and 25 CBP molecules in the cube, the planar CBP host molecules tended to aggregate more easily and more significantly than the TCTA molecules (Figure 3d; Figures S21–S24, Supporting Information). These MD simulation results are supported by DFT calculations, which show that the intermolecular interaction energy of CBP (-0.268 eV) is substantially larger in magnitude than that of TCTA (-0.083 eV) (Figures S25 and S26, Supporting Information). This difference accounts for the higher aggregation propensity of CBP. Thermal annealing further exacerbates this aggregation and promotes crystallization, ultimately accelerating device degradation due to the low thermal stability and planar, easily packable structure of CBP (Figures S27–S29, Tables S3 and S4, Supporting Information).

When comparing the operational stability of fabricated SOLEDs, the improved charge balance of the TCTA:CBP mixed-host device without thermal annealing (“as-spun”) had a longer T_{50} ($\approx 105\text{ h}$) than did the TCTA single-host device ($\approx 21\text{ h}$)

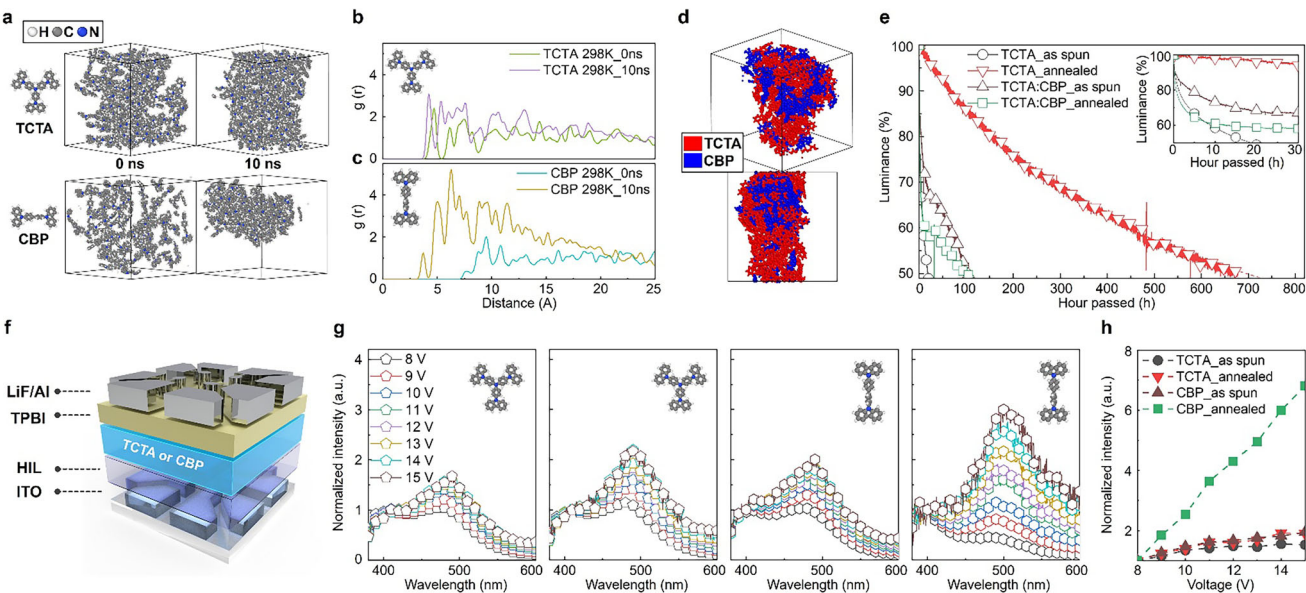


Figure 3. a) Distribution of TCTA and CBP molecules before and after 10 ns simulated by molecular dynamics at 298 K. Radial distribution function of the distances between the centers-of-mass for b) TCTA and c) CBP before and after 10 ns at 298 K (insets: molecular structures). d) 3D and side view of molecular distribution of TCTA:CBP mixed-host EML film in a 1:1 ratio after 10 ns at 298 K. e) Luminance-decay over time of SOLEDs using TCTA single-host and TCTA:CBP mixed-host with or without thermal treatment. f) Schematic illustration of device structure of SOLEDs without guest molecules. g) Normalized electroluminescence spectra of SOLEDs without guest molecules (EML: TCTA as spun, TCTA annealed at 110 °C, CBP as spun, and CBP annealed at 110 °C). h) Evolution of normalized EL peak intensity with various applied bias.

(Figure 3e; Figure S30, Supporting Information). However, thermal annealing of the TCTA:CBP mixed-host film shortened the T_{50} of the device (to ≈ 99 h), as a result of severe molecular aggregation of CBP. The device that used as-spun TCTA single-host EML had very low operational stability (Figure 3e; Figures S1 and S2, Supporting Information), but the annealed film had improved molecular packing, which improved charge transport, decreased the number of charge traps related to the residual solvent or voids within the film, and improved the charge balance; consequently, the T_{50} increased significantly to ≈ 702 h (Figure 3e; Figures S30 and S31, Table S5, Supporting Information).

To directly observe the formation of electromers in the EML under electrical driving and thermal treatment, devices were fabricated without phosphorescent guest molecules (Figure 3f). The driving voltage V_D was increased from 8 to 15 V, while the electroluminescence (EL) spectra of the devices were traced. As V_D increases, devices that used TCTA:CBP had a significant increase in EL intensity at a wavelength $\lambda \approx 500$ nm, which corresponds to the formation of electromers that is induced by molecular aggregates formation as the V_D is increased; in contrast, the devices that used only TCTA showed a relatively small change in the intensity of the electromer-related EL peak at ≈ 490 nm (Figure 3g,h).

Comparison of the PL of films that contained only host (TCTA or TCTA:CBP) or host: 2,2',2''-(1,3,5-Benzinetriyl)-tris(1-phenyl-1-H-benzimidazole) (TPBI) indicated that these peaks represent the formation of complexes between aggregated TCTA or CBP host electromers and TPBI at the host/ETL (i.e., TPBI) interface in the device (Figures S32 and S33, Supporting Information). In a device that had the structure anode/HIL/CBP/cathode, when comparing the PL and EL spectra, an electromer peak

at ≈ 600 nm, which is not observed in the PL (Figure S34, Supporting Information), rises in the EL spectrum as V_D increases (Figure S35, Supporting Information), so this peak is confirmed to be due to the formation of CBP aggregates or of their electromers.

As the concentration of charge traps increases as a consequence of electromer formation from thermally-annealed CBP molecules, exciton-polaron interactions and exciton quenching by polarons become increasingly severe, and thereby accelerate the degradation in device EL properties, especially operational stability.^[42] Conversely, exciton-polaron interactions can induce host aggregation.^[21,25] These continuous interactions between molecular aggregation and exciton quenching further exacerbate device deterioration, and significantly reduce operational lifetime.

2.3. Hole-Injection Interface

Because fabrication of multilayered SOLEDs is challenging, a large hole-injection energy barrier generally forms between the HIL and the EML in SOLEDs. Therefore, the electrical and electronic properties of the hole-injection material, as well as its hole-injection characteristics, significantly influence the efficiency and stability of devices.^[19,20]

To study the influence of the material properties of the HIL and the characteristics of the hole injection interface that forms at the HIL/EML on SOLED devices, a comparative analysis was conducted using the conventional polymeric HIL (PEDOT:PSS), and the self-organized polymeric HIL (SO-HIL). The SO-HIL is composed of PEDOT:PSS and a perfluorinated sulfonic acid (PFSA) that has a lower surface energy and higher IP than PEDOT and

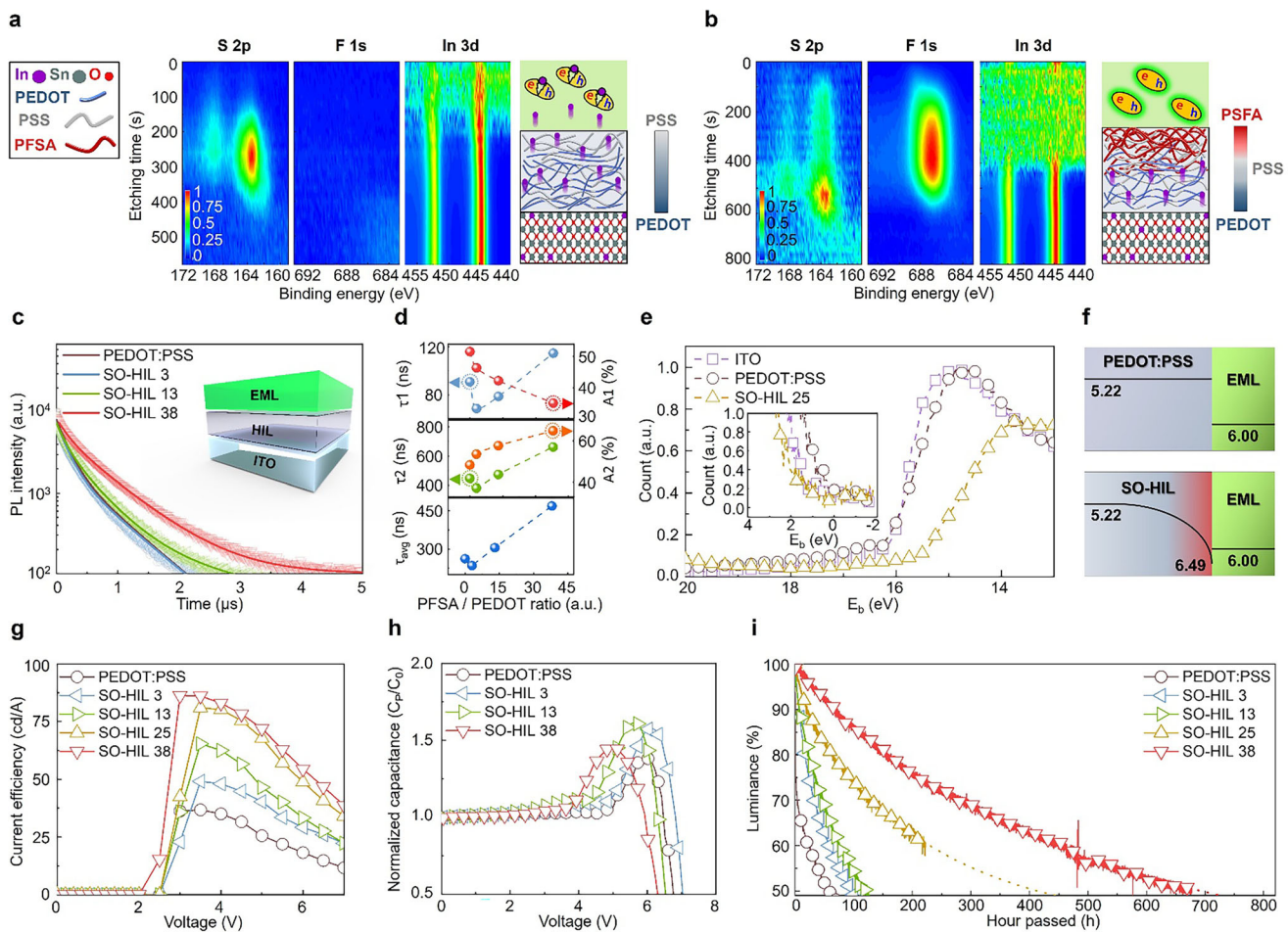


Figure 4. Depth profile of X-ray photoelectron spectroscopy (XPS) for S 2p, F 1s, and In 3d and schematic illustration of exciton quenching in EML by diffused metal species with a) PEDOT:PSS and b) SO-HIL. c) Time-resolved photoluminescence (TRPL) spectra of ITO/HIL/EML films using various hole injection layers; the number following “SO-HIL” represents the weight ratio of PFSA to PEDOT. d) PL lifetime from TRPL decay curves depending on PFSA/PEDOT ratio. e) Ultraviolet photoelectron spectroscopy spectra of ITO, PEDOT:PSS and SO-HIL 25. f) Schematic energy band diagram of HIL/EML with PEDOT:PSS or SO-HIL. g) Current efficiency versus voltage, h) normalized capacitance versus voltage, and i) luminance-decay over time of TCTA single-host SOLEDs with 15 wt% Ir(mppy)₃ guest using various PFSA/PEDOT ratio in HIL.

PSS;^[23,28] this trait enables spontaneous self-organization during film forming solution process (Figures S36 and S37, Supporting Information). PFSA chains, which have lower surface energy than the PEDOT and PSS chains, preferentially migrate to the top surface of the HIL film, and thereby develop a gradient work function that increases from the anode toward EML (Figure 4a,b).^[20,28,43–46] Generally, acidic PEDOT:PSS (1.0 ≤ pH ≤ 2.5)^[26,27] readily etches the underlying ITO; this process releases metallic atoms such as In and Sn, and their ions, that can diffuse into overlying layers.^[28] These metal species migrate through the HIL and reach the EML, where they impede carrier injection and degrade device performance by trapping carriers and inducing nonradiative exciton recombination.^[28] The self-organized, surface-enriched PFSA layer in the SO-HIL can efficiently block diffusion of metal atoms to the proximity of the EML.

This molecular self-assembly and effective metal blocking were confirmed by X-ray photoelectron spectroscopy (XPS) depth profiling (Figure 4a,b). In ITO/PEDOT:PSS/EML film, diffused In was distributed throughout the entire HIL and even detected

within the EML (Figure 4a; Figure S38, Supporting Information). In contrast, SO-HIL films showed surface enrichment of PFSA, as evidenced by the fluorine concentration profile, and no In species was detected above the PFSA-rich region (Figure 4b). These results demonstrate that the self-assembled PFSA layer effectively prevents metal diffusion toward the EML, thereby mitigating charge trapping and exciton quenching, ultimately enhancing both efficiency and stability.

PEDOT:PSS is also a strong exciton quencher in OLEDs.^[23] Efficient blocking of non-radiative exciton recombination caused by diffusion of metal atoms and by PEDOT:PSS was demonstrated by steady-state and time-resolved PL analysis of ITO/HIL/EML films (Figure 4c,d; Figure S39, Table S6, Supporting Information). The number following SO-HIL represents the weight ratio of PFSA to PEDOT (PFSA/PEDOT). The gradual increase in PL lifetimes from 262.75 ns on the PEDOT:PSS to 469.95 ns on the SO-HIL that contained a PFSA/PEDOT:PSS weight ratio of 38 (SO-HIL 38) suggests a gradual reduction in exciton quenching at the interface due to formation of a self-organized PFSA layer,

which keeps excitons away from the quenching interface.^[23] Furthermore, this molecular self-assembly results in a high surface IP due to the surface-concentrated perfluorinated polymer chains that have high IP. Ultraviolet photoelectron spectroscopy revealed that the surface IP of the SO-HIL 25 is as high as 6.49 eV, whereas conventional PEDOT:PSS has a relatively low surface IP of 5.22 eV (Figure 4e,f). The gradient work function, which increases from ITO toward the EML, effectively injects holes into the EML that has a high HOMO energy level of \approx 6.1 eV by the Fowler-Nordheim tunneling process, which reduces the height of the energy barrier at the HIL/EML interface.^[23,47] As a result, the luminous efficiency of SOLEDs gradually increased as the relative composition of PFSA increased in the HIL (Figure 4g; Figure S40, Supporting Information), from CE = 36.76 cd A⁻¹ in the device that used PEDOT:PSS as HIL, to 86.26 cd A⁻¹ in the device that used SO-HIL 38. The increase in PFSA composition leads to hole injection at lower voltage (lower V_{th}), and more efficient recombination (lower V_{peak}), as evidenced by the C-V characterizations (Figure 4h). Most importantly, the increase in PFSA extended the T₅₀ of the SOLEDs significantly from \approx 59 h with the PEDOT:PSS to \approx 702 h with SO-HIL 38 (Figure 4i). Ineffective hole injection causes accumulation both of holes and excess electrons that cannot recombine with injected holes in the EML.^[19] Increased charge trapping and exciton annihilation at the interface critically limit the operational stability of SOLEDs by promoting non-radiative decay and irreversible chemical degradation in the EML.^[19,48,49] Trapped carriers disrupt charge balance and intensify exciton-exciton and exciton-polaron interactions, leading to localized bond scission, defect formation, and molecular decomposition.^[20,50,51] These processes accelerate the formation of deep trap states that act as additional quenching centers, initiating a feedback loop of degradation.

2.4. Operational Characteristics of SOLED

The operational degradation characteristics of SOLEDs were investigated by analyzing C-V and transient EL characteristics of devices. Ir(ppy)₃, with its shallower HOMO level, directly captures holes from the HIL and exhibits severe aggregation, leading to charge imbalance. In contrast, Ir(ppy)₂(acac) has better energy alignment with the host and remains well-dispersed in the EML. Operational characteristics and charge carrier behavior changes due to degradation showed distinct trends in SOLEDs that used Ir(ppy)₃ or Ir(ppy)₂(acac) (Figure 5a,b; Figure S41, Supporting Information). In the initial devices, the direct hole trapping into Ir(ppy)₃ enabled earlier charge injection at lower voltages, which reflected in lower V_{th} in C-V characteristics than in devices that used Ir(ppy)₂(acac) (Figure 5a). However, in degraded devices in which the luminance has decreased to \approx 50% of its initial value under constant current operation (L₅₀), the charge injection in Ir(ppy)₃ SOLEDs is significantly degraded compared to Ir(ppy)₂(acac) devices. As a result, in the Ir(ppy)₃ SOLEDs, the V_{peak} increased substantially (4.87 to 5.82 V), while C_{peak}/C₀ decreased from 1.49 to 1.11. In contrast, in the L₅₀ SOLED with Ir(ppy)₂(acac), the V_{peak} was slightly delayed from 4.32 to 4.78 V, and C_{peak}/C₀ decreased only slightly from 1.38 to 1.25, which changes were significantly smaller than in the Ir(ppy)₃ SOLEDs (Figure 5a; Figure S41a, Supporting Information).

Similarly, the SOLED that used Ir(ppy)₃ initially showed a very short EL delay and fast EL rise under a square pulse of applied voltage (delay time, t_d \approx 0.02 ms, rising time, t_r defined as the time required to reach 80% of the saturated EL intensity \approx 0.35 ms) due to direct charge injection, but these were significantly lengthened after degradation (t_d \approx 0.50 ms, t_r \approx 7.10 ms) (Figure 5b; Figure S41b, Supporting Information). In contrast, the SOLED that used Ir(ppy)₂(acac) showed minimal changes in charge injection, transport, and the position of the recombination region during device operation, so these times changed only minimally (fresh device: t_d \approx 0.38 ms, t_r \approx 4.15 ms; degraded device: t_d \approx 0.56 ms, t_r \approx 5.6 ms) (Figure 5b; Figure S41b, Supporting Information). The SOLED that used Ir(mppy)₃ also showed no significant changes in charge injection, transport, and recombination behavior during device operation, demonstrated by C-V and transient EL characterizations (Figure S42, Supporting Information).

The combination of the molecular properties of the host and thermal treatment of the solution-processed film also influences the degradation dynamics (Figure 5c,d; Figure S43, Supporting Information). In SOLEDs without thermal annealing of the emitter film ("as spun" devices), SOLEDs that used a TCTA:CBP mixed-host EML achieve a better charge balance than TCTA single-host, which increases the operational stability of the SOLED due to the reduction of accumulated charges in the device.^[19,20] As a result, the changes in t_d and t_r are less significant in the SOLEDs that used TCTA:CBP mixed-host EMLs than in SOLEDs that used a TCTA single-host; this comparison indicates that the changes in charge injection, transport, and recombination characteristics are less affected by device operation in the SOLEDs that used TCTA:CBP mixed-host EMLs than in SOLEDs that used a TCTA single-host (Figure 5c,d; Figure S43, Supporting Information).

However, thermal annealing of solution-processed organic small molecule films alters the morphological, electrical, and photophysical properties of these two organic emitter thin films, so their behavior during device operation changes. The thermal treatment leads to formation of molecular aggregates, and this process degrades the photophysical properties of the EML film rather than improving the electrical properties of the thin film (Figures S15, S27 and S30, Supporting Information). Additionally, charge traps are more readily formed in the TCTA:CBP than in TCTA due to the aggregates and spatial voids created by the strong molecular aggregation of CBPs.

As a result, thermal annealing of the TCTA single-host EML device, causes smaller changes in V_{th}, V_{peak}, C_{peak}, t_d and t_r than in SOLEDs that used unannealed film during device operation (Figure 5c,d; Figures S43 and S44, Supporting Information). However, thermal annealing of TCTA:CBP mixed EML film caused larger differences V_{th}, V_{peak}, C_{peak}, t_d and t_r than in SOLEDs that used unannealed film; this comparison indicates that device operation leads to more significant changes in charge injection, transport, and recombination characteristics in these thermally annealed mixed-host devices than in unannealed device (Figure 5c,d; Figures S43, S45 and 46, Supporting Information).

The characteristics of hole injection, in combination with the properties of the solution-processed EML in SOLEDs, create a significant synergistic effect that determines the device's

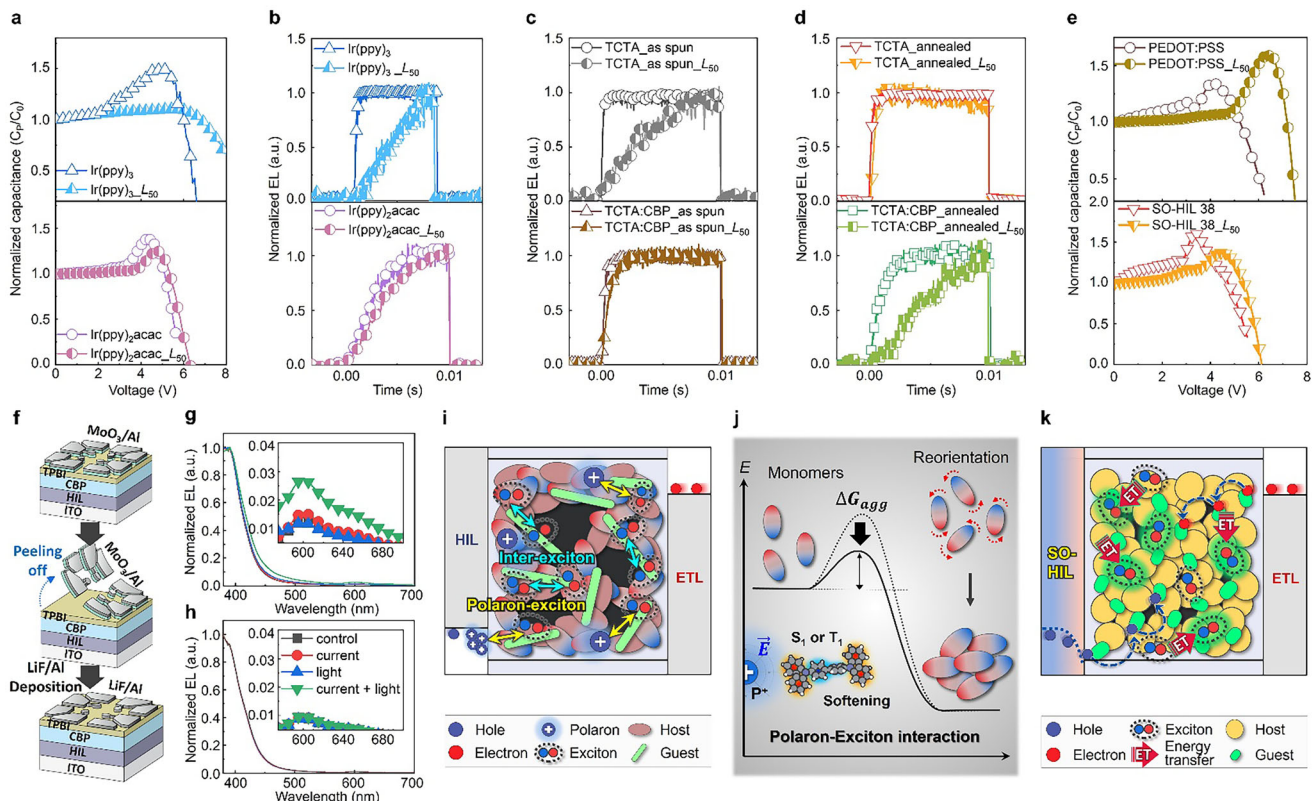


Figure 5. a) Normalized capacitance versus voltage (C-V), b) transient electroluminescence (EL) characteristics before and after device degradation of TCTA:CBP mixed-host SOLEDs using Ir(ppy)₃ or Ir(ppy)₂(acac). Transient EL rising characteristics of SOLEDs using TCTA single-host or TCTA:CBP mixed-host c) without and d) with thermal treatment according to device degradation. e) C-V characteristics of SOLEDs using PEDOT:PSS and SO-HIL 38 before and after device degradation. f) Schematic illustrations of device structures of SOLEDs without guest molecules, showing the process of peeling off and replacing the metal electrodes. Normalized EL spectra of g) PEDOT:PSS and h) SO-HIL based devices before and after current or light stress. i) Schematic illustrations of self-reinforcing degradation mechanism of SOLEDs using conventional HIL, host and guest molecules with high intermolecular interactions. j) Schematic illustrations of molecular aggregation triggered by exciton-polaron coexistence, which induces molecular softening and lowers energy barrier for aggregation. k) Schematic illustrations of efficient recombination and stable device operation of SOLEDs using high IP SO-HIL, host and guest molecules with reduced intermolecular interactions.

operational behavior and degradation dynamics. SOLED that used SO-HIL lower the energy barrier height for hole injection formed with the EML (Figure 4f), which enables improved charge injection, as can be confirmed by the lower V_{th} and V_{peak} in C-V characteristics in SOLEDs that used SO-HIL than in SOLEDs that use PEDOT:PSS (Figure 5e). Additionally, the surface-enriched insulating self-organized PFSA part of SO-HIL strengthens electron blocking, and thereby effectively confines charges and yields a higher C_{peak} but a more efficient recombination process, as indicated by the steeper decrease in capacitance after V_{peak} than in SOLED that used PEDOT:PSS (Figure 5e).

Degradation of SOLED that used PEDOT:PSS, causes significant increases in V_{th} (from 3.43 to 5.03 V), and V_{peak} (from 4.13 to 6.32 V), which indicate significant degradation of hole injection capability at the HIL/EML interface, and substantial increases in both the turn-on voltage and operating voltage of the SOLED. In contrast, use of a SO-HIL, even as the device degrades, showed much smaller increases in V_{th} (from 2.94 to 3.53 V) and V_{peak} (from 3.33 to 4.43 V) than with PEDOT:PSS (Figure 5e).

In the case of PEDOT:PSS, a large capacitance developed even at high voltages; this result indicates charge accumulation due

to a severe imbalance in charge injection/transport. In contrast, even at the same level of degradation, SO-HIL showed fast reduction in capacitance; this response indicates that the devices underwent efficient charge recombination and maintained charge balance relatively well even at high voltages (Figure 5e). These results show that the characteristics of the HIL and the HIL/EML interface are key factors that determine the device's luminous efficiency (Figure 4g) and operational lifetime (Figure 4i), and they also influence the rate of variation in charge carrier imbalance, which are caused by changes in charge injection, transport, and recombination characteristics during operation.

To probe the role of exciton-polaron interactions in driving interfacial aggregation, we designed a stress-and-readout experiment using hole-only devices (ITO/HIL/CBP/TPBi/MoO₃/Al), which were subjected to four distinct preconditioning conditions: (i) no stress, (ii) electrical bias only (polaron generation), (iii) UV light only (exciton generation), and (iv) simultaneous bias and light exposure (coexistence of polarons and excitons) (Figure 5f). After stress, the top electrode was removed and replaced with LiF/Al to allow electron injection and EL readout. Only under condition (iv), PEDOT:PSS-based device exhibited a new emission

peak near 600 nm, indicating aggregation induced by exciton-polaron coexistence (Figure 5g; Figures S32–S35, Supporting Information). In contrast, SO-HIL devices showed minimal spectral changes under all conditions, consistent with suppressed polaron accumulation (Figure 5h). These results provide direct evidence that interfacial aggregation is electrostatically triggered by the spatial overlap of excitons and polarons, and can be mitigated through improved hole-injection energetics.

2.5. Self-Reinforcing Degradation Mechanism of SOLEDs

The analyses in this study reveal that the self-reinforcing degradation of SOLEDs proceeds through synergistic effects among multiple processes:

- i. *guest aggregation and charge trapping*: direct charge trapping by guest molecules and their intermolecular aggregation in solution-processed films promote the accumulation of excited species (polarons, bipolarons, and excitons) within guest-rich regions. This localized accumulation increases the probability of exciton-polaron and exciton-exciton interactions, accelerating nonradiative decay (Figure 5i).
- ii. *host aggregation and morphological defects*: thermal annealing or operational stress induces aggregation and partial crystallization of planar and low- T_g host molecules, leading to molecular packing and void formation in the film. These morphological defects enhance charge carrier trapping and facilitate further exciton-polaron interactions.
- iii. *synergistic impact of hole injection*: a large hole injection barrier at the HIL/EML interface leads to hole accumulation, triggering intensified exciton-polaron interactions at the interface or at the proximity of the interface, further enhanced molecular aggregation, and rapid degradation of SOLEDs.
- iv. *fundamental origin of molecular aggregation in SOLEDs*: the spatial coexistence of excitons and polarons induces strong local electric field gradients within the EML (Figure S47, Supporting Information). These fields polarize nearby molecules and enhance their local polarizability, particularly in excited states with enlarged transition dipole moments (Figure S48, Supporting Information). This interaction softens the molecular potential surface and reduces the free energy barrier for aggregation (ΔG_{agg}), promoting molecular reorganization and $\pi\text{-}\pi$ stacking even in initially amorphous domains (Figure 5j). Moreover, energy transfer from excitons to accumulated polarons at the HIL/EML interface may produce excited polaronic states (P_+^*), which are energetically unstable, further accelerating local morphological disruption (Figure 5j; Figures S49 and S50, Supporting Information).
- v. *self-reinforcing exciton-polaron interactions*: in SOLEDs, a large hole injection barrier leads to the accumulation of positive polarons at the HIL/EML interface. Spatial overlap between these polarons and nearby excitons induces local electric fields, which increase the polarizability and mobility of surrounding molecules. This promotes molecular aggregation, with the resulting aggregates forming additional charge traps and polaronic states that further enhancing exciton-polaron interactions.

This sets “self-reinforcing cycle”: inefficient hole injection → polaron accumulation → exciton-polaron interaction → excited polaron → molecular aggregation → further imbalance and degradation.

Conversely, when guest and host aggregation are effectively suppressed, hole injection is efficient, and charge accumulation is minimized through appropriate material selection and interface engineering, the degradation feedback loop can be inhibited. In this case, SOLEDs exhibit high luminous efficiency, reduced nonradiative losses, and significantly improved operational stability (Figure 5k).

3. Conclusion

In this study, we systematically investigated the key factors that influence the degradation and operational stability of SOLEDs. By analyzing molecular interactions, charge balance, and interface properties, we established a comprehensive understanding of the degradation mechanisms that affect SOLEDs, and provided strategies to increase their efficiency and lifespan. Our findings highlight the synergistic role of excited-state interactions and molecular interactions in device degradation. Additionally, we identified a self-reinforcing degradation pathway in SOLEDs, by which charge accumulation and exciton-polaron interactions induce molecular aggregation, which in turn increases charge trapping and exciton annihilation. This cycle is particularly pronounced in devices that have inefficient hole injection, because accumulated holes at the HIL/EML interface interact with excitons concentrated in EML; this process leads to polaron-induced aggregation and further degradation of charge-transport properties. By employing low-interaction guests, spherical and high- T_g hosts, and optimized HILs, this detrimental cycle can be effectively suppressed, leading to significantly improved operational stability.

Overall, our study underscores the importance of materials combination and interface engineering in optimizing SOLED stability. By appropriately designing guest molecules, host materials, and HIL compositions, we provide a strategy to increase the luminous efficiency and operational lifetime of SOLEDs simultaneously. These insights will contribute to the development of commercially-viable SOLED technologies for next-generation display and lighting applications.

4. Experimental Section

Device Fabrication: Glass substrate patterned with Indium-tin-oxide (ITO) was sequentially sonicated in acetone and isopropyl alcohol (IPA) for 15 min each, then treated with UV-ozone for 20 min. Polymeric hole-injection layer (HIL) was then spin-coated on the glass/ITO substrates. The SO-HIL was prepared by mixing PEDOT:PSS (Clevios P VP Al 4083; PEDOT:PSS ratio = 1:6 wt:wt) with tetrafluoroethylene-perfluoro-3,6-dioxa-4-methyl-7 octene-sulfonic acid copolymer (Sigma Aldrich) at various mass ratios. The substrates were then annealed at 150 °C for 30 min. Substrates were transferred to a nitrogen-filled glove box, in which the emitting layer was spin-coated onto the HIL film at 4000 rpm for 60 s. The emitting layer solution was prepared by dissolving host and guest molecules in tetrahydrofuran (THF, anhydrous, ≥ 99.9%, Sigma-Aldrich). TCTA and CBP were purchased from OSM and Ir(ppy)₃, Ir(ppy)₂(acac), and Ir(mppy)₃ were obtained from Nichem Fine Technology. The emitting layer was either processed without annealing or thermally annealed at 70 or 110 °C

for 30 min. Finally, the SOLED devices were completed by sequential vacuum deposition of TPBi (50 nm, >99.9%, OSM) as the ETL, LiF (1 nm, ≥99.99%, Sigma-Aldrich) and Al (100 nm, Itasco) under high vacuum ($\leq 5.0 \times 10^{-7}$ Torr).

Device Characterizations: Current-voltage-luminance (J-V-L) characteristics and luminous efficiencies (LE) of SOLEDs were measured using a source-measurement unit (Keithley 2400), photodiode (SM05PD1A, Thorlabs) and spectrometer (avaSpec-ULS2048CL-EVO RS, Avantes). Operational lifetimes of the SOLEDs were measured using an OLED lifetime tester (M600 plus, McScience). Capacitance-voltage (C–V) characteristics were measured using an electrochemical impedance spectroscope (Bio-logic SP-300), applying a voltage sweep from 0 to 10 V at a constant frequency of 1000 Hz. Steady-state photoluminescence (PL) measurements were conducted using Jasco FP-8500 fluorometer with a xenon lamp as the light source, and a Pico Quant Fluotime 300 equipped with a 405 nm laser. Time-resolved photoluminescence (TRPL) measurements were performed using the Pico Quant Fluotime 300 equipped with a 405 nm laser. Refractive indexes of films were measured using a spectroscopic ellipsometer (Elli-SE(UV)-FM8, Ellips Technology). Transient electroluminescence characteristics were measured using a pulse generator (hp 8116A, 90 ms; 10 Hz frequency), photomultiplier tube (PMTSS, Thorlabs) and oscilloscope (Agilent infiniium 54832D MSO). Surface morphology was analyzed using an atomic force microscope (AFM, XE 100, PARK SYSTEMS). Ultraviolet photoelectron spectroscopy (UPS) measurements were conducted using a Thetaprobe (Thermo) equipped with a He I (21.2 eV) source, with a –10 eV bias applied to the sample. X-ray photoelectron spectroscopy (K-Alpha plus, Thermo Scientific) was conducted using a monochromatic Al K α source (1486.6 eV). Depth profiling was conducted by Ar $^+$ sputtering (1 keV, 70 s).

Density Functional Theory: DFT calculations were performed using both Gaussian 16 and the Vienna Ab initio Simulation Package (VASP). Gaussian 16 was used to calculate the electrostatic potential and the dipole moment of molecules, using the B3LYP functional with the 6-31G(d) basis set for non-metal atoms and the LANL2DZ effective core potential for the Ir atoms. VASP was used to calculate intermolecular interaction energy with the projector augmented-wave method and generalized gradient approximation (GGA) within the Perdew-Burke-Ernzerhof (PBE) framework. Grimme's DFT-D2 method was applied for van der Waals corrections. The plane-wave basis set was expanded to a cutoff energy of 400 eV to minimize Pulay stress during the structural optimization. The structural optimization was truncated until the Hellmann-Feynman forces were < 0.03 eV Å $^{-1}$. Electronic energy convergence was set to 1×10^{-5} eV.

Molecular Dynamics: All molecular dynamics (MD) simulations were performed using the Large-scale Atomic/Molecular Massively Parallel Simulator (LAMMPS). The interaction parameters for TCTA and CBP were generated using the Automated Topology Builder (ATB) by considering the GROMOS 54A7 force field. A 1.4-nm cut-off was applied for non-bonded interactions. Each simulation was conducted in a cube (5.0 × 5.0 × 5.0 nm) with periodic boundary conditions. Three systems were prepared, each containing 50 molecules: pure TCTA, pure CBP, and a 1:1 mixture of TCTA and CBP. The simulations were run at 298 K and 393 K under the NVT ensemble for 10 ns with a 1-fs time step, and temperature was controlled using the Bussi-Donadio-Parrinello thermostat. Radial distribution functions (RDFs) were then calculated after a 10-ns equilibration.

Supporting Information

Supporting Information is available from the Wiley Online Library or from the author.

Acknowledgements

E.C. and J.J. contributed equally to this work. This work was supported by the National Research Foundation of Korea (NRF) grant funded by the Korean government (Ministry of Science and ICT, MSIT) (RS-2025-00558546, RS-2024-00411892, RS-2024-00446129), and by LG Display Co., Ltd. under the Incubation Program at Hanyang University (C2025001523).

Conflict of Interest

The authors declare no conflict of interest.

Data Availability Statement

The data that support the findings of this study are available from the corresponding author upon reasonable request.

Keywords

charge injection, degradation, organic light-emitting diodes, solution process

Received: April 1, 2025

Revised: June 21, 2025

Published online: July 4, 2025

- [1] J.-Y. Woo, M.-H. Park, S.-H. Jeong, Y.-H. Kim, B. Kim, T.-W. Lee, T.-H. Han, *Adv. Mater.* **2023**, 35, 2207454.
- [2] L. Duan, L. Hou, T.-W. Lee, J. Qiao, D. Zhang, G. Dong, L. Wang, Y. Qiu, *J. Mater. Chem.* **2010**, 20, 6392.
- [3] A. Monkman, *ACS Appl. Mater. Interfaces* **2022**, 14, 20463.
- [4] F. Hermerschmidt, S. A. Choulis, E. J. W. List-Kratochvil, *Adv. Mater. Technol.* **2019**, 4, 1800474.
- [5] S. Wang, Y. C. Wu, S. Jiao, T. Shi, N. Ai, Y. Zhang, S. Iguchi, P. Y. Lu, H. Zhou, *SID Symp. Dig. Tech. Pap.* **2019**, 50, 1157.
- [6] S. Meyer, S. Stolz, M. Hamburger, H. R. Tseng, M. Engel, A. Hayer, R. Linge, S. Tierney, G. Bernatz, R. Anémian, *SID Symp. Dig. Tech. Pap.* **2020**, 51, 391.
- [7] S. Stolz, S. Meyer, A. Hayer, R. Linge, M. Engel, L. I. Rodríguez, M. Hamburger, H. R. Tseng, A. Jatsch, R. Anémian, *SID Symp. Dig. Tech. Pap.* **2021**, 52, 264.
- [8] T.-H. Han, M.-R. Choi, C.-W. Jeon, Y.-H. Kim, S.-K. Kwon, T.-W. Lee, *Sci. Adv.* **2016**, 2, 1601428.
- [9] Y.-H. Kim, C. Wolf, H. Cho, S.-H. Jeong, T.-W. Lee, *Adv. Mater.* **2016**, 28, 734.
- [10] Y.-H. Kim, T.-H. Han, C. Lee, Y.-H. Kim, Y. Yang, T.-W. Lee, *Adv. Funct. Mater.* **2020**, 30, 2011003.
- [11] M. R. Nagar, A. Choudhury, D. Tavgeniene, R. Beresneviciute, D. Blazevicius, V. Jankauskas, K. Kumar, S. Banik, S. Ghosh, S. Grigalevicius, J.-H. Jou, *J. Mater. Chem. C* **2022**, 10, 3593.
- [12] R. Kumaresan, H.-Y. Park, A. Maheshwaran, H. Park, Y. Do, M. Song, J. Yoon, S. Il Ahn, S.-H. Jin, *Adv. Opt. Mater.* **2022**, 10, 6.
- [13] N. Li, Z. Chen, C. Zhou, F. Ni, Z. Huang, X. Cao, C. Yang, *Adv. Mater.* **2023**, 35, 2300510.
- [14] K. Kumar, K. K. Kesavan, S. Kumar, F. R. Chen, A. Karmakar, J. Jayakumar, R. Goswami, S. Banik, J.-H. Jou, S. Ghosh, *J. Phys. Chem. C* **2023**, 127, 18560.
- [15] Y. Yin, X. Lai, Q. Ma, H. Ma, W. Zhu, J.-Y. Lee, Y. Wang, *Adv. Mater.* **2024**, 36, 2313656.
- [16] X. Zhuang, B. Liang, C. Jiang, S. Wang, H. Bi, Y. Wang, *Adv. Opt. Mater.* **2024**, 12, 2400490.
- [17] S. Wu, D. Chen, X. H. Zhang, D. Sun, E. Zysman-Colman, *Adv. Mater.* **2025**, 37, 2415289.
- [18] C. Murawski, K. Leo, M. C. Gather, *Adv. Mater.* **2013**, 25, 6801.
- [19] T.-H. Han, W. Song, T.-W. Lee, *ACS Appl. Mater. Interfaces* **2015**, 7, 3117.
- [20] T.-H. Han, Y.-H. Kim, M.-H. Kim, W. Song, T.-W. Lee, *ACS Appl. Mater. Interfaces* **2016**, 8, 6152.
- [21] Q. Wang, B. Sun, H. Aziz, *Adv. Funct. Mater.* **2014**, 24, 2975.

- [22] H. Yu, Y. Zhang, Y.-J. Cho, H. Aziz, *ACS Appl. Mater. Interfaces* **2017**, 9, 14145.
- [23] T.-H. Han, M.-R. Choi, S.-H. Woo, S.-Y. Min, C.-L. Lee, T.-W. Lee, *Adv. Mater.* **2012**, 24, 1487.
- [24] T.-W. Lee, T. Noh, H.-W. Shin, O. Kwon, J. J. Park, B.-K. Choi, M.-S. Kim, D.-W. Shin, Y.-R. Kim, *Adv. Funct. Mater.* **2009**, 19, 1625.
- [25] Y.-J. Cho, S. Taylor, H. Aziz, *ACS Appl. Mater. Interfaces* **2017**, 9, 40564.
- [26] C. Liu, M. Li, Y. Wang, Z. Hou, J. Chen, K. Cao, L. Liu, S. Chen, *ACS Appl. Mater. Interfaces* **2024**, 16, 62469.
- [27] J. Cameron, P. J. Skabara, *Mater. Horiz.* **2020**, 7, 1759.
- [28] T.-H. Han, Y. Lee, M.-R. Choi, S.-H. Woo, S.-H. Bae, B.-H. Hong, J.-H. Ahn, T.-W. Lee, *Nat. Photonics* **2012**, 6, 105.
- [29] S. Reineke, T. C. Rosenow, B. Lüssem, K. Leo, *Adv. Mater.* **2010**, 22, 3189.
- [30] Z. Gao, F. Wang, K. Guo, H. Wang, B. Wei, B. Xu, *Opt. Laser Technol.* **2014**, 56, 20.
- [31] V. Shrotriya, Y. Yang, *J. Appl. Phys.* **2005**, 97.
- [32] M. C. Jung, J. Facendola, J. Kim, D. S. Muthiah Ravinson, P. I. Djurovich, S. R. Forrest, M. E. Thompson, *Adv. Mater.* **2021**, 33, 2102882.
- [33] K.-H. Kim, J.-J. Kim, *Adv. Mater.* **2018**, 30, 1705600.
- [34] A. B. Kajjam, S. Vaidyanathan, *Chem. Rec.* **2018**, 18, 293.
- [35] C.-H. Lee, J.-H. Lee, K.-H. Kim, J.-J. Kim, *Adv. Funct. Mater.* **2018**, 28, 1800380.
- [36] M.-W. Ha, M.-H. Park, J.-Y. Hwang, J. Kim, D.-H. Kim, T.-W. Lee, Y.-H. Kim, *Dyes Pigm.* **2021**, 185, 108880.
- [37] Q. Wang, H. Aziz, *ACS Appl. Mater. Interfaces* **2013**, 5, 8733.
- [38] S. Liu, C. Peng, A. Cruz, Y. Chen, F. So, *J. Mater. Chem. C* **2016**, 4, 8696.
- [39] Y.-J. Cho, H. Aziz, *ACS Appl. Mater. Interfaces* **2018**, 10, 18113.
- [40] J. A. McEwan, A. J. Clulow, A. Nelson, N. R. Yepuri, P. L. Burn, I. R. Gentle, *ACS Appl. Mater. Interfaces* **2017**, 9, 14153.
- [41] M.-H. Tsai, Y.-H. Hong, C.-H. Chang, H.-C. Su, C.-C. Wu, A. Matoliukstyte, J. Simokaitiene, S. Grigalevicius, J. V. Grazulevicius, C.-P. Hsu, *Adv. Mater.* **2007**, 19, 862.
- [42] Y. J. Cho, Y. Zhang, H. Yu, H. Aziz, *Adv. Funct. Mater.* **2016**, 26, 8662.
- [43] T.-H. Han, M.-H. Park, S.-J. Kwon, S.-H. Bae, H.-K. Seo, H. Cho, J.-H. Ahn, T.-W. Lee, *NPG Asia Mater.* **2016**, 8, 303.
- [44] S. Ahn, S.-H. Jeong, T.-H. Han, T.-W. Lee, *Adv. Opt. Mater.* **2017**, 5, 1600512.
- [45] S. Ahn, T.-H. Han, K. Maleski, J. Song, Y.-H. Kim, M.-H. Park, H. Zhou, S. Yoo, Y. Gogotsi, T.-W. Lee, *Adv. Mater.* **2020**, 32, 2000919.
- [46] J. W. Jang, J. Y. Woo, C. B. Lee, W. D. Kim, J. Park, D. Kim, Y. Zhao, J.-S. Yeo, M. G. Kim, S. H. Nam, S. H. Lee, Y.-H. Kim, D. R. Lee, Y. Yang, K. Kim, T.-H. Han, *ACS Energy Lett.* **2024**, 9, 6029.
- [47] I. D. Parker, *J. Appl. Phys.* **1994**, 75, 1656.
- [48] R. Meerheim, S. Scholz, S. Olthof, G. Schwartz, S. Reineke, K. Walzer, K. Leo, *J. Appl. Phys.* **2008**, 104, 014510.
- [49] D. Y. Kondakov, J. R. Sandifer, C. W. Tang, R. H. Young, *J. Appl. Phys.* **2003**, 93, 1108.
- [50] S. Kim, H. J. Bae, S. Park, W. Kim, J. Kim, J. S. Kim, Y. Jung, S. Sul, S.-G. Ihn, C. Noh, S. Kim, Y. You, *Nat. Commun.* **2018**, 91, 1211.
- [51] S. Schmidbauer, A. Hohenleutner, B. König, *Adv. Mater.* **2013**, 25, 2114.